

A VLT/FORS2 Narrowband Imaging Search for Mg II Emission Around $z \sim 0.7$ Galaxies

RYAN RICKARDS VAUGHT,^{1,2} KATE H. R. RUBIN,¹ FABRIZIO ARRIGONI BATTALIA,³ J. XAVIER PROCHASKA,⁴ AND JOSEPH F. HENNAWI⁵

¹*Department of Astronomy, San Diego State University, San Diego, CA 92182, USA*

²*Department of Physics, University of California, San Diego, 9500 Gilman Dr., La Jolla, CA 92093, USA*

³*European Southern Observatory, Karl-Schwarzschild-Str. 2, D-85748 Garching bei München, Germany*

⁴*Department of Astronomy & Astrophysics, University of California, 1156 High Street, Santa Cruz, CA 95064, USA*

⁵*Department of Physics, Broida Hall, University of California, Santa Barbara, CA 93106, USA*

ABSTRACT

We perform a Very Large Telescope FOCal Reducer and low dispersion Spectrograph 2 (VLT/FORS2) narrowband imaging search around 5 star-forming galaxies at redshift $z = 0.67 - 0.69$ in the Great Observatories Origins Deep Survey South (GOODS-S) field to constrain the radial extent of large-scale outflows traced by resonantly scattered Mg II emission. The sample galaxies span star formation rates in the range $4 M_{\odot} \text{ yr}^{-1} < \text{SFR} < 40 M_{\odot} \text{ yr}^{-1}$ and have stellar masses $9.9 \lesssim \log M_{*}/M_{\odot} \lesssim 11.0$, and exhibit outflows traced by Mg II absorption with velocities $\sim 150 - 420 \text{ km s}^{-1}$. These observations are uniquely sensitive, reaching surface brightness limits of $5.81 \times 10^{-19} \text{ ergs sec}^{-1} \text{ cm}^{-2} \text{ arcsec}^{-2}$ per 1 arcsec^2 aperture (at 5σ significance). We do not detect any extended emission around any of the sample galaxies, thus placing upper limits on the brightness of extended Mg II emission of $< 6.51 \times 10^{-19} \text{ ergs sec}^{-1} \text{ cm}^{-2} \text{ arcsec}^{-2}$ at projected distances $R_{\perp} > 8 - 21 \text{ kpc}$. The imaging also resolves the Mg II absorption observed toward each galaxy spatially, revealing approximately constant absorption strengths across the galaxy disks. In concert with radiative transfer models predicting the surface brightness of Mg II emission for a variety of simple wind morphologies, our detection limits suggest that either (1) the extent of the Mg II-emitting material in the outflows from these galaxies is limited to $\lesssim 20 \text{ kpc}$; or (2) the outflows are anisotropic and/or dusty.

Keywords: galaxies: evolution – galaxies: halo

1. INTRODUCTION

Galactic winds play a critical role in regulating the star formation rates and stellar masses of galaxies (Werk et al. 2014); however, the physics that powers these winds remains uncertain. Some possible mechanisms have been proposed by theoretical studies that include thermal pressure from core collapse supernovae, radiation pressure from starbursts, and finally cosmic ray pressure (e.g., Larson 1974; Chevalier & Clegg 1985; Springel & Hernquist 2003; Sugahara et al. 2017). Additionally, the impact galactic winds have on their host galaxies (i.e., their mass and energy content) has remained difficult to constrain with observations.

An accurate picture of the types of galaxies that host outflows comes from numerous absorption line studies

of galaxies (e.g., Veilleux et al. 2005; Weiner et al. 2009; Martin et al. 2012; Rubin et al. 2014). Gas flows are detected by measuring the blueshift (outflow) or redshift (inflow) of absorption transitions with respect to the host galaxy systemic velocity. Spectroscopy of galaxies from low to high redshifts probing cold gas ($T \lesssim 10^2 \text{ K}$) which absorbs in Na I and cool gas ($T \sim 10^4 \text{ K}$) absorbing Mg II has revealed outflows in most galaxies that host active star formation (e.g. Chen et al. 2010; Martin et al. 2012; Rubin et al. 2014). While this technique is useful for constraining the radial velocity, column density and covering fraction of the flow, it weakly constrains the overall radial extent and provides little information on the morphology of the gas.

An alternative method that can in principle assess the radial extent and morphology of outflows is to trace the gas in emission. This has been demonstrated using rest-frame optical transitions (i.e., H α , [O III]) as tracers for winds around nearby starbursts (e.g., Matsubayashi

et al. 2009; Veilleux et al. 2009) as these transitions can trace the warm shock-heated phase of the gas. Another transition potentially useful for tracing winds in emission is the Mg II $\lambda\lambda 2976, 2803$ doublet in the rest-frame ultraviolet (UV; Weiner et al. 2009; Kornei et al. 2013). While most studies of winds using Mg II have focused on its absorption kinematics, Rubin et al. (2011) observed strong Mg II emission with a P-Cygni line profile in the spectrum of a strongly star-forming galaxy at redshift $z = 0.694$. In addition, the emission was spatially extended, permitting the first direct measurement of the extent of an outflow ($\gtrsim 7$ kpc) in the distant universe.

One proposed production mechanism for such P-Cygni profiles is photon scattering. In this mechanism, Mg II ions in the region of the wind closest to the observer will absorb continuum photons in the resonant transitions at wavelengths 2796.35\AA (λ_{2796}) and 2803.53\AA (λ_{2803}) (Morton 2003). Once these transitions are excited, they may only decay back to the ground state. If the optical depth of the gas is high, then the gas will resonantly trap the absorbed photons. Because the photons are absorbed in the rest frame of the gas, the absorption will be blueshifted relative to the galaxy’s systemic velocity. The Mg II ions in the section of the wind farthest from the observer will absorb and scatter photons that are redshifted relative to the front portion of the wind. Because the photons are redshifted, the photons travel freely towards the observer through the wind to produce emission at and redward of the systemic velocity of the galaxy (Rubin et al. 2011, Prochaska et al. 2011).

Since the first detection of Mg II emission in an individual galaxy by Rubin et al. (2011), another detection was reported by Martin et al. (2013), who observed Mg II emission that extends $12 - 18$ kpc from a strongly star-forming galaxy at $z = 0.9392$. Mg II has also been studied in wide-field galaxy surveys conducted with the Keck DEep Imaging Multi-Object Spectrograph (DEIMOS) and the VLT Multi Unit Spectroscopic Explorer (MUSE) (Weiner et al. 2009, Kornei et al. 2013, Erb et al. 2012, Feltre et al. 2018). These surveys, which include galaxies with redshifts $0.70 < z < 2.30$, find that Mg II may be detected in pure emission, pure absorption or with P-Cygni profiles and that detections of Mg II in emission were found to be more commonly associated with galaxies of lower stellar mass and with bluer spectral slopes.

The diversity of these spectral profiles may be understood using radiative transfer modeling of galactic winds. Prochaska et al. (2011) have used this technique to predict spectra for the Mg II and Fe II* fine-structure transitions for a variety of wind morphologies. The authors demonstrated that isotropic dust-

free winds will conserve photon flux, thus predicting that blueshifted absorption lines should be accompanied by emission lines with similar equivalent widths (EW). Anisotropic winds, however, were demonstrated to exhibit significantly weaker emission by a factor proportional to the angular extent (i.e., solid angle) of the wind. Scattered emission was found to be additionally weakened by the inclusion of dust and the presence of a strongly-absorbing interstellar medium (ISM). Thus, spatially-resolved measurement of the surface brightness of this emission constrains not only the radial extent of the emitting material, but also its morphology and dust content.

In this paper, we present the first narrowband imaging of the Mg II transition around 5 star-forming galaxies located in the Great Observatories Origins Deep Survey South (GOODS-S; Giavalisco et al. 2004) field at redshift $z \sim 0.7$. We use two filters: a “line filter” covering the Mg II doublet, and a “continuum filter” that is offset from the line filter by ~ 47 Å. The resulting imaging in each filter has a total integration time of 10 hrs. As opposed to 1D spectra, the narrowband imaging constrains the surface brightness and radial extent of the wind. These observations allow us to create the first ever high-S/N spatially resolved map of both Mg II emission and absorption.

In Section 2 we describe our sample of GOODS-S galaxies, supplemental Keck I Low Resolution Imaging Spectrometer (Keck/LRIS) spectra, as well as our VLT/FORS2 observations, image reduction, and absolute flux calibration. We describe our method of continuum subtraction in Section 3. Analysis of these data is presented in Section 4, including our methods for calculating surface brightness profiles and detection limits for each galaxy, as well as maps of Mg II equivalent widths. Section 5 presents results from this analysis. We compare our SB detection limits to previous detections of extended Mg II emission, and compare our observations to predictions made using radiative transfer models in Section 6. We conclude this paper in Section 7. We adopt a Λ CDM cosmology with $h_{70} = H_0/(70 \text{ km s}^{-1} \text{ Mpc}^{-1})$, $\Omega_M = 0.3$, and $\Omega_\Lambda = 0.7$. In this cosmology, $1''$ is ≈ 7 kpc at $z \sim 0.7$.

2. OBSERVATIONS AND DATA REDUCTION

2.1. Sample Selection

Our target galaxies were selected from a Keck/LRIS survey of UV absorption lines in ≈ 100 objects having redshifts $0.3 < z < 1.4$ and rest-frame B -band magnitudes $B_{AB} < 23$ in fields with deep Hubble Space Telescope/Advanced Camera for Surveys (*HST*/ACS) imaging (Rubin et al. 2014). In particular, this parent survey

targeted galaxies in a total of nine Keck/LRIS pointings located in both of the GOODS fields (Giavalisco et al. 2004) and the AEGIS survey field (the Extended Groth Strip; Davis et al. 2007). In inspecting the redshift distribution of the portion of this sample observable from the Southern Hemisphere, we uncovered a narrow peak of nine galaxies in the interval $0.66 \lesssim z \lesssim 0.68$. This peak is in fact the global maximum of the distribution, as all other bins of width $\Delta z = 0.02$ have at most four galaxies. Moreover, there are two narrow interference filters available on VLT/FORS2 centered at $\lambda \sim 4675 \text{ \AA}$ and 4722 \AA which cover the Mg II $\lambda\lambda 2796, 2803$ transition in precisely this redshift interval. We selected our final sample of five of these galaxies to be close on the sky such that they could be imaged in a single $7' \times 7'$ FORS2 pointing. We show color *HST*/ACS images of these objects in Figure 1.

The absorption line modeling presented in Rubin et al. (2014) indicates that these five galaxies are driving strong outflows traced by Mg II with velocities $\sim 150 - 420 \text{ km s}^{-1}$ and equivalent widths (EW) $\sim 2 - 3 \text{ \AA}$. Modeling of the galaxy broad-band spectral energy distributions (SEDs) obtained from multi-wavelength ancillary imaging data yields star formation rates (SFR) ranging from ~ 4 to $40 M_{\odot} \text{ yr}^{-1}$ and stellar masses in the range $\log M_*/M_{\odot} \sim 9.9 - 11.0$. The properties of the sample, as well as precise target coordinates taken from Rubin et al. (2014), are listed in Table 1.

2.2. VLT/FORS2 Observations

Our narrow-band imaging data were taken in service mode using the FORS2 instrument on the VLT 8.2m telescope Antu between October 2012 and February 2013. We used two narrowband filters, HeII+47 and HeII/3000+48, that have peak transmission at wavelengths that correspond to the Mg II doublet lines at our sample redshift of $z \sim 0.7$ (see Table 2). The filter transmission curves are plotted along with each galaxy’s spectrum in Figure 2. In the following, we will often refer to the HeII+47 filter as the “line” or Mg II filter and the HeII/3000+48 filter as the “continuum” filter.

FORS2 has a native pixel scale of $0.125'' \text{ pixel}^{-1}$ and a field of view of $7' \times 7'$. The data were taken with the CCD binned 2×2 , yielding a pixel scale of $0.25'' \text{ pixel}^{-1}$. Images of three pointings offset by $0.25'$ East/West were obtained, with individual exposure times of $\approx 1000 \text{ sec}$. A total of 38 exposures were taken in each filter. Our observations were carried out under photometric and thin cloud conditions (program ID: 090.A-0427A). The seeing values, given in the header of each image, were derived from zenith observations at 0.5 micron with the Paranal differential image motion monitor (DIMM; Sarazin &

Roddier 1990) and include a correction for the airmass and wavelengths of the science observations, as well as a first order correction for the larger size of the Antu mirror. The distribution of these seeing values is shown in Figure 3. The median seeing for the images is $\sim 0.8''$. Summing the individual exposure times for each filter results in a combined exposure time of 10.0 hours each for the HeII+47 and HeII/3000+48 images.

2.3. Supplemental Keck/LRIS spectra

In addition to VLT imaging, in the present analysis we utilize galaxy spectra taken from the Rubin et al. (2014) Keck/LRIS program. A $0.9''$ slit width was used for all slitmasks and the median FWHM resolution for the spectra is 274 km s^{-1} at $\lambda_{\text{rest}} \approx 2800 \text{ \AA}$ and 286 km s^{-1} at $\lambda_{\text{rest}} \approx 2600 \text{ \AA}$ (see Figure 2). The spectral coverage of these data extends from ~ 3200 to 8000 \AA .

2.4. Image Reduction

The imaging data were fully reduced using custom routines written in *Python*. The images were first corrected by subtracting and removing the overscan region of the CCD. Then the images were bias-subtracted and flat-fielded using twilight flats. An additional flat-fielding correction was performed using night-sky flats to improve our sensitivity to faint extended emission. The night-sky flats were produced by first masking out all objects and bad pixels in the science frames, and then combining them using an average sigma-clipping algorithm. Cosmic rays and bad pixels in the science images are removed by utilizing the *L. A. Cosmic* algorithm (van Dokkum 2001). The astrometry solutions were calculated via Astrometry.net (Lang et al. 2010), and yield a standard deviation in the galaxy coordinates of $\sigma \approx 0.10''$. Before image stacking, we ran each frame through *SExtractor* (Bertin et al. 1996) to create a root mean square (RMS) map of each science image.

The final stacked image for each filter is obtained using *SWarp* (Bertin et al. 1996). Each individual frame is first sky-subtracted using a background mesh size of 256 pixels which is approximately $64''$. We chose the mesh size to be large enough such that any extended emission is not mistakenly subtracted (e.g., Arrigoni Battaia et al. 2015). The frames, after background-subtraction, are resampled onto a common astrometric solution using a *Lanczos3* interpolation kernel. The images are weighted by the night-flat image and then average-combined to increase the signal-to-noise of any Mg II emission. Additionally, *SWarp* generates stacked RMS images by propagating the error images for each science frame. Our final stacked images in each filter are shown in Figure 4 with the target galaxies indicated.

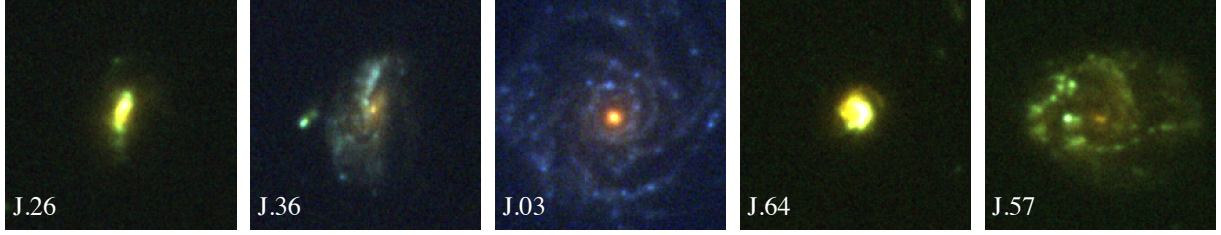


Figure 1. Color imaging of our sample galaxies in the *HST*/ACS F435W, F606W, and F775W filters obtained as part of the GOODS survey (Giavalisco et al. 2004). Each image is $5'' \times 5''$ (or about $35 \text{ kpc} \times 35 \text{ kpc}$).

Table 1. Properties of the 5 galaxies in our sample as estimated in Rubin et al. (2014). The EW (in the observed frame) includes both components of the Mg II doublet and is determined from analysis of the supplemental Keck/LRIS spectra.

Object	R.A.	Dec	z	$\log(\text{SFR})$ ($\log M_{\odot} \text{ yr}^{-1}$)	$\log(M)$ ($\log M_{*}/M_{\odot}$)	EW_{obs} (\AA)	τ_V
J033225.26-274524.0 (J.26)	03:32:25.26	-27:45:23.9	0.6660	$9.1^{+1.3}_{-3.7}$	$9.86^{+0.05}_{-0.04}$	7.539 ± 0.354	$1.227^{+1.54}_{-0.20}$
J033231.36-274725.0 (J.36)	03:32:31.35	-27:47:24.9	0.6669	$10.5^{+1.7}_{-1.6}$	$10.02^{+0.03}_{-0.03}$	5.835 ± 0.493	$1.377^{+0.60}_{-0.23}$
J033230.03-274347.3 (J.03)	03:32:30.03	-27:43:47.2	0.6679	3.8^{+0}_{-0}	$10.98^{+0.01}_{-0.0}$	12.794 ± 1.710	$0.297^{+0.0}_{-0.0}$
J033229.64-274242.6 (J.64)	03:32:29.64	-27:42:42.5	0.6671	$40.5^{+8.2}_{-12.1}$	$10.30^{+0.07}_{-0.03}$	13.239 ± 0.263	$3.897^{+1.15}_{-0.93}$
J033230.57-274518.2 (J.57)	03:32:30.56	-27:45:18.2	0.6807	$12.6^{+1.7}_{-2.1}$	$10.48^{+0.03}_{-0.07}$	6.106 ± 0.370	$1.262^{+1.23}_{-0.40}$

NOTE—The uncertainty intervals reported for SFR, $\log M_{*}/M_{\odot}$, and τ_V values indicate the ± 34 th-percentile values of the posterior probability distribution function of each quantity as determined via modeling of the objects' SEDs with MAGPHYS (da Cunha et al. 2008, 2012) as described in Rubin et al. (2014)

Table 2. Filter properties and exposure times of the VLT/FORS2 observations. The widths of the transmission curves ($\Delta\lambda$) are calculated by convolving the transmission curves over the total wavelength range of each filter. These values differ slightly from those reported by the European Southern Observatory.

Filter (Line)	λ_{eff}^a (\AA)	$\Delta\lambda^b$ (\AA)	N^c	T^d (S)	S^e
HeII+47 (Mg II)	4675.21	50.11	38	35,959	2.45
HeII/3000+48 (Cont.)	4722.46	44.82	38	36,937	2.40

^a λ_{eff} is the effective wavelength of the filter transmission curve.

^b FWHM of the filter.

^c Total number of images.

^d Total exposure time.

^e S , the sensitivity of the filter, is in units of $10^{-17} \text{ ergs counts}^{-1} \text{ cm}^{-2}$.

2.5. Absolute Flux Calibration

We acquired observations of the standard star GD50 from archival ESO calibration imaging at 4 independent epochs. Performing aperture photometry at each epoch and airmass, we calculated the atmospheric extinction coefficients, k , to be 0.181 magnitudes for the HeII/3000+48 filter and 0.190 magnitudes for the HeII+47 filter. We perform absolute flux calibration using the methods of Jacoby et al. (1987). We first convolve the spectral energy distribution of the standard star, $F(\lambda)$ in $\text{ergs sec}^{-1} \text{ \AA}^{-1} \text{ cm}^{-2}$, with that of the known transmission curve of the filter, $T_i(\lambda)$. This yields F_i , the total observable flux in each bandpass filter i with units of $\text{ergs sec}^{-1} \text{ cm}^{-2}$:

$$F_i = \int F(\lambda) T_i(\lambda) d\lambda.$$

It is not uncommon to assume that $F(\lambda)$ is constant over the small width of the filter. However, since our filter transmission curves are sampled at wavelengths similar to sampling of the spectrum of GD50 from the the CALSPEC library (Bohlin et al. 2017), we interpolate both spectra and compute the integral without the constant $F(\lambda)$ assumption. The conversion from count rate to

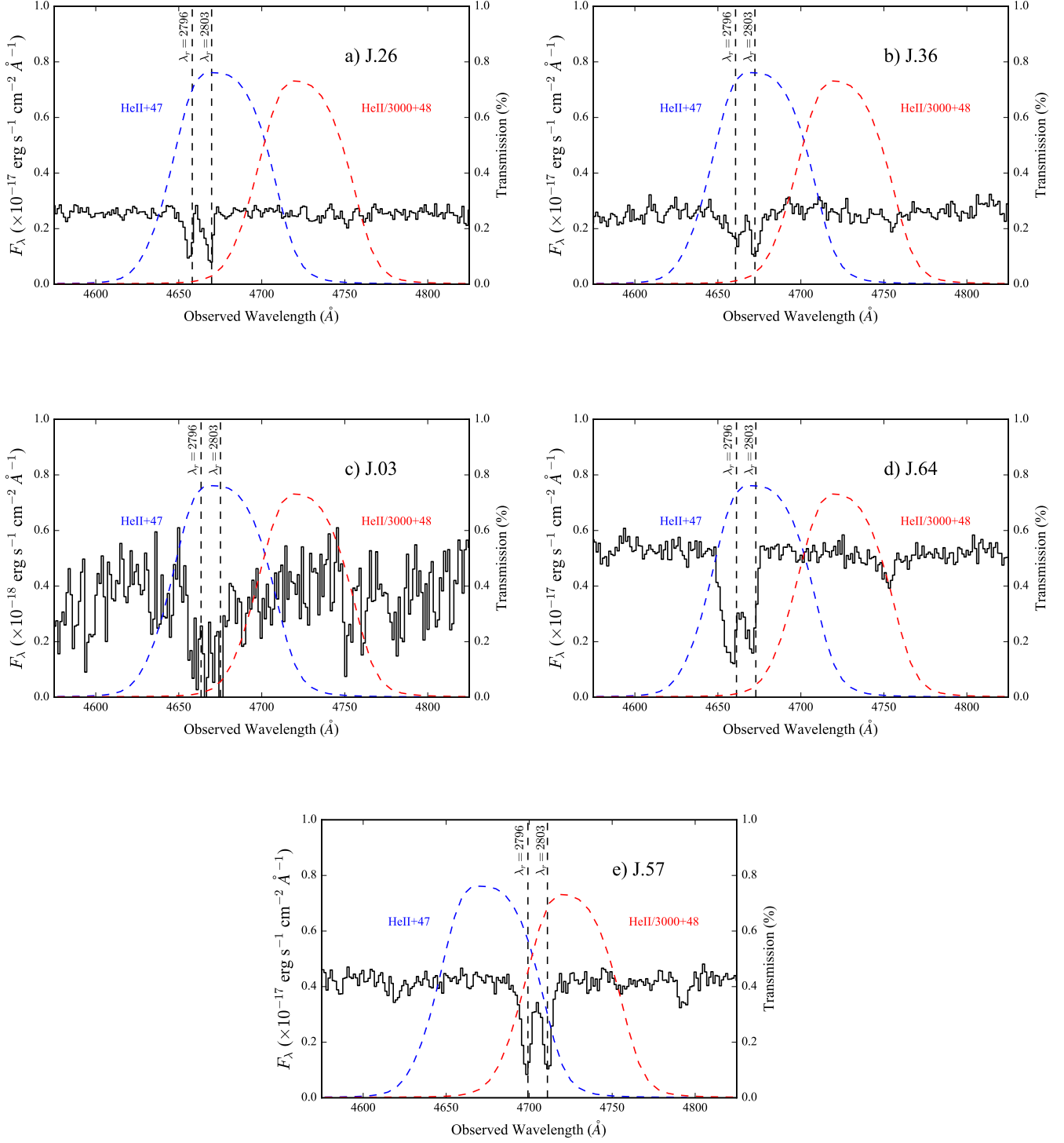


Figure 2. Keck/LRIS spectra of the sample galaxies and the transmission curves of the filters HeII+47 (blue dashed line) and HeII/3000+48 (red dashed line). The left-hand axis is in units of flux density and the right-hand axis is the percentage of light transmitted by the filter at each wavelength. Vertical dashed lines indicate the wavelengths of the redshifted Mg II doublet. The Mg II doublet falls fortuitously at the central wavelength of the HeII+47 filter for the galaxies shown in panels (a) through (d).

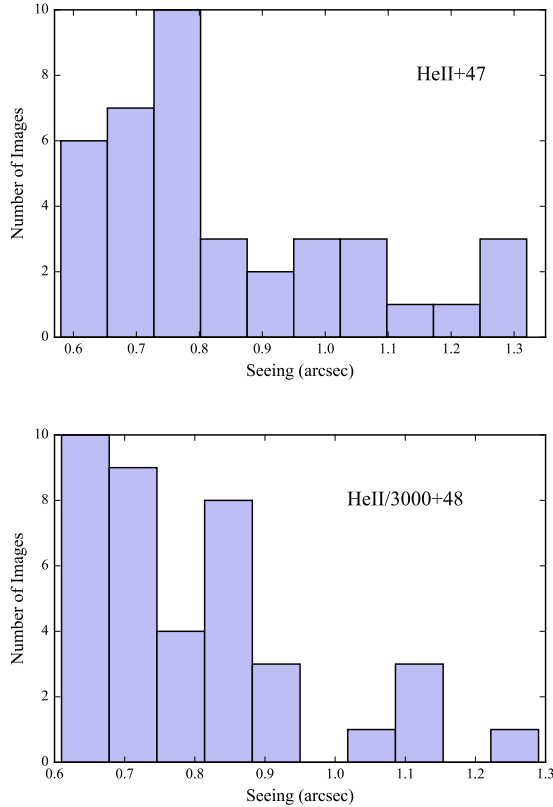


Figure 3. Top: Distribution of seeing measurements for the 38 HeII+47 images. **Bottom:** Same for the HeII/3000+48 images. The median seeing value for the images in both filters is $\sim 0.8''$. The seeing conditions were calculated from DIMM measurements which are provided by ESO in the header of each science image.

flux units for each filter is then given by

$$S_i = \frac{F_i}{C10^{k_i A}},$$

where k_i is the extinction in magnitudes per airmass, A is the airmass for each individual exposure, C is the measured count rate of the standard star and S_i is in units of $\text{ergs counts}^{-1} \text{cm}^{-2}$. Before image co-addition, each science image is corrected for atmospheric extinction by multiplying each frame by $10^{k_i A}$. Next, the image is divided by the exposure time, effectively putting the image in units of counts per sec. After co-addition, the images are then multiplied by the appropriate sensitivity factor S_i . This puts the final images in the appropriate flux units, $\text{ergs sec}^{-1} \text{cm}^{-2}$.

3. IMAGE SUBTRACTION

We have two goals for our study: (1) assess the surface brightness of line emission in the Mg II transition

in and around each target galaxy; and (2) spatially resolve the morphology of the strong Mg II absorption observed against the galaxy continua. To achieve both of these goals, we must perform accurate subtraction of the continuum flux of each object from the images taken with the filter covering the targeted line emission. For four of the five galaxies in our sample, the HeII+47 image includes both line and continuum emission, and the HeII3000+48 image provides a high S/N measurement of the continuum only $\approx 30 \text{ \AA}$ redward of the line emission in the rest frame. The spectral coverage of these filters is qualitatively different for the fifth galaxy in our sample (J.57). As shown in Figure 2, the Mg II transitions in this galaxy are equally sampled by both of our filters. When we subtract the continuum image from the Mg II image we are effectively subtracting both Mg II emission (if present) and the continuum. We thus use this galaxy as check on the quality of our continuum subtraction.

3.1. Spectral Correction

In preparation for continuum subtraction, we first consider whether the continuum level of each galaxy spectrum changes significantly over the passbands of our two filters. We use the supplementary spectra from Rubin et al. (2014) to fit the continuum and determine the spectral slope of each galaxy. We use the interactive fitting routine *lt_continuumfit* from the *linetools* package (Prochaska 2016)¹ to fit the continuum. We then find the total continuum flux in each filter by convolving the fitted continuum with each filter’s transmission curve. Next, we take the ratio of both integrated totals, as the ratio will indicate the scaling factor needed to correct our flux measurements prior to continuum subtraction.

Comparing these ratios between each galaxy, we find that they are equivalent to within 0.1%, with a value of 1.118. This value is equal to the ratio between the FWHMs of the filter transmission curves, indicating that the spectral slope of each galaxy is approximately flat, and that the continuum level measured in the off-line filter provides an accurate measure of the continuum contribution to the on-line filter flux.

3.2. Continuum Subtraction

To properly continuum-subtract the image taken with the Mg II filter, we follow a prescription given by Arigoni Battaia et al. (2015). We first determine the continuum flux density from the continuum filter,

$$f_{\text{cont}} = \frac{F_{\text{cont}}}{\Delta\lambda_{\text{cont}}}, \quad (1)$$

¹ <https://github.com/linetools/linetools>

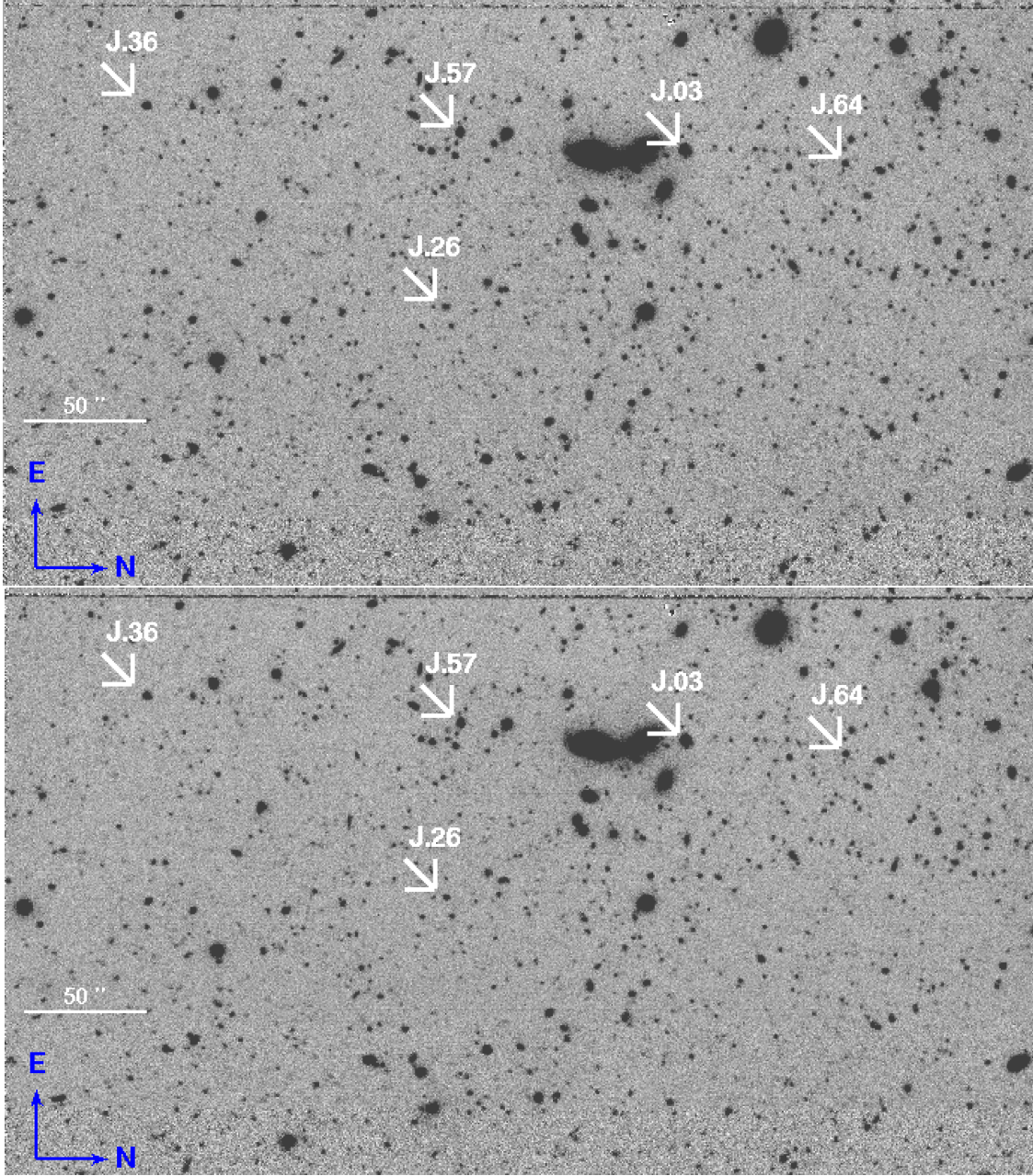


Figure 4. Top: Stacked HeII+47 image of the galaxy sample. Bottom: Stacked HeII3000+48 image of the same pointing. The exposure time of each image is ≈ 10 hours. Each image shows half of the total FOV ($7' \times 5'$), which contains the full sample of galaxies (indicated by the white arrows). East is up and North is right.

where F_{cont} and $\Delta\lambda_{\text{cont}}$ are the observed flux per pixel of the continuum image and the transmission FWHM of the continuum filter, respectively. With f_{cont} it is then possible to calculate the flux of any excess emission, F_{line} :

$$F_{\text{line}} = F_{\text{MgII}} - f_{\text{cont}}\Delta\lambda_{\text{MgII}} \quad (2)$$

where F_{MgII} and $\Delta\lambda_{\text{MgII}}$ are the observed flux per pixel in the Mg II filter and the transmission FWHM of the Mg II filter. The continuum-subtracted images of

each galaxy are shown in Figure 5. The continuum-subtracted image has uniform background and no obvious signatures of emission.

4. ANALYSIS

4.1. Surface Brightness Profiles and Limits

To test for the presence of Mg II emission, we perform aperture photometry on the continuum-subtracted images using the python library *Photutils*. We choose annuli with a radial thickness of 1 pixel or $0.25''$, such

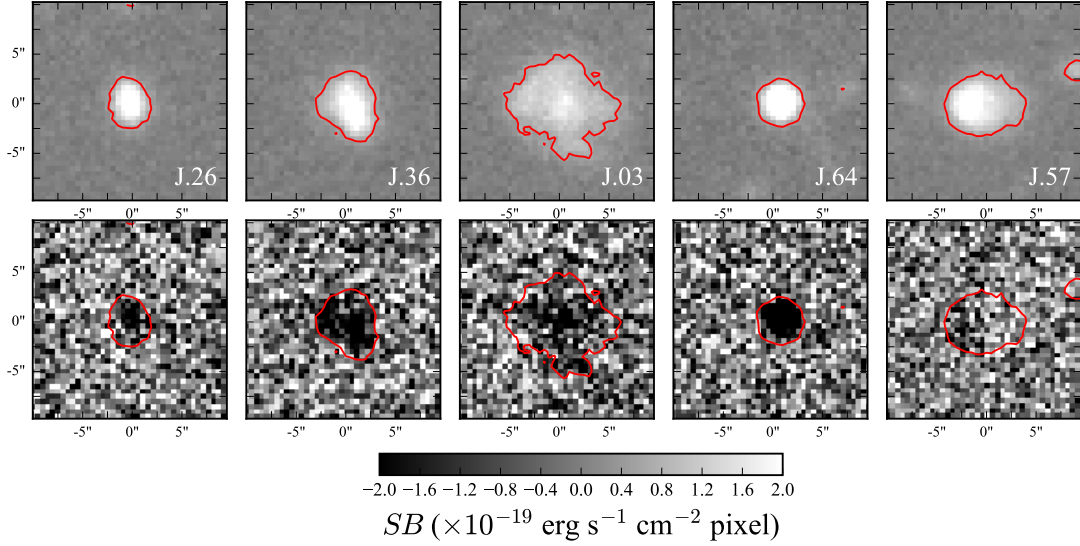


Figure 5. $10'' \times 10''$ (or about $70 \text{ kpc} \times 70 \text{ kpc}$) images of each galaxy in our sample. Top row: Continuum surface brightness in $\text{ergs s}^{-1} \text{ cm}^{-2} \text{ pixel}$, measured in the HeII/3000+48 filter. Bottom row: Continuum-subtracted Mg II surface brightness. Absorption can be seen in 4 of 5 galaxies. The red contours represent the outline of the 1σ surface brightness limit in the HeII+47 image, defined in Sec. 4.1. The colorbar shows the scaling used for the bottom row Mg II images.

that $r_{\text{inner}} = r_{\text{outer}} - 1$ (in pixels). Each annulus is centered on the flux-weighted centroid of the galaxy. By dividing the summed flux in each annulus by the area in arcseconds we produce surface brightness (SB) profiles for each galaxy. These profiles are shown in Figure 6.

The error in the SB is determined from the stacked RMS images of each object. We adopt annuli that are identical to the annuli used to find the SB profiles for each galaxy. To calculate the variance inside each annulus, we sum the RMS pixel values in quadrature, then divide by the area of each annulus.

To calculate the 1σ SB limit we follow the procedure of Arrigoni Battaia et al. (2015). We first mask out all the sources, their associated extended halos, and edge noise in both the HeII+47 and HeII/3000+48 images. We then calculate the RMS of the background in randomly-placed $1''$ apertures. We convert these RMS values to SB limits per 1 arcsec^2 aperture. We find that the 1σ detection limits (SB_1) are $6.332 \times 10^{-19} \text{ ergs sec}^{-1} \text{ cm}^{-2} \text{ arcsec}^2$ and $5.808 \times 10^{-19} \text{ ergs sec}^{-1} \text{ cm}^{-2} \text{ arcsec}^2$ in the HeII/3000+48 and HeII+47 filters, respectively. With the 1σ detection limit, SB_1 , determined for the continuum+Mg II (HeII+47) image, we define a thicker (or “extended”) annulus to be used to search for any extended Mg II emission. This annulus will have an inner radius approximately the size of the SB_1 isophotal contour for each galaxy. The outer radius is chosen to be the inner radius plus 5 pixels. With this larger annulus, we can average any flux over large areas to reach lower SB. The mean radii of these extended apertures are 18, 18, 24 and 21 kpc from the centers of the targets

J.26, J.36, J.03 and J.64, respectively. The resulting SB measurements are shown in Figure 6.

In the case of perfect sky subtraction and continuum subtraction, the 1σ SB limit for an extended source is $SB_1/\sqrt{A_{\text{src}}}$, where A_{src} is the area in arcsec^2 and SB_1 is the surface brightness limit per 1 arcsec^2 aperture. However, our actual detection limits are altered by systematic error from imperfect subtraction. Therefore, we determine the limits as follows. We first mask all the artifacts and sources in the continuum-subtracted images. Next, we generate many apertures with sizes similar to our extended annulus ($\sim 20 \text{ sq.arcsec}$), place them at random, and extract the fluxes, F_{src} , within these apertures. We then normalize the values of F_{src} by dividing by σ_{src} , where $\sigma_{\text{src}} \equiv SB_1\sqrt{A_{\text{src}}}$. For perfect sky subtraction and continuum subtraction, the distribution of extracted fluxes should follow a Gaussian distribution with a variance equal to σ_{src} . The distribution of $F_{\text{src}}/\sigma_{\text{src}}$ for these apertures is shown in Figure 7

We calculate the variance and mean of the distribution and find that the variance of the distribution is $\sigma'_{\text{src}} = 1.1$, implying that the SB detection limit for our continuum-subtracted image is higher than σ_{src} by a factor of 10%. We adopt $F_{\text{limit}} \equiv \sigma'_{\text{src}}$ as the 1σ upper limit on the total line flux of extended Mg II emission. The SB_{limit} is then $F_{\text{limit}}/A_{\text{src}}$. The values of F_{src} and $5SB_{\text{limit}}$ for each galaxy are listed in Table 3.

4.2. Test of Surface Brightness Limits

To show that Mg II emission with SB strengths comparable to our limits can be detected in our narrowband

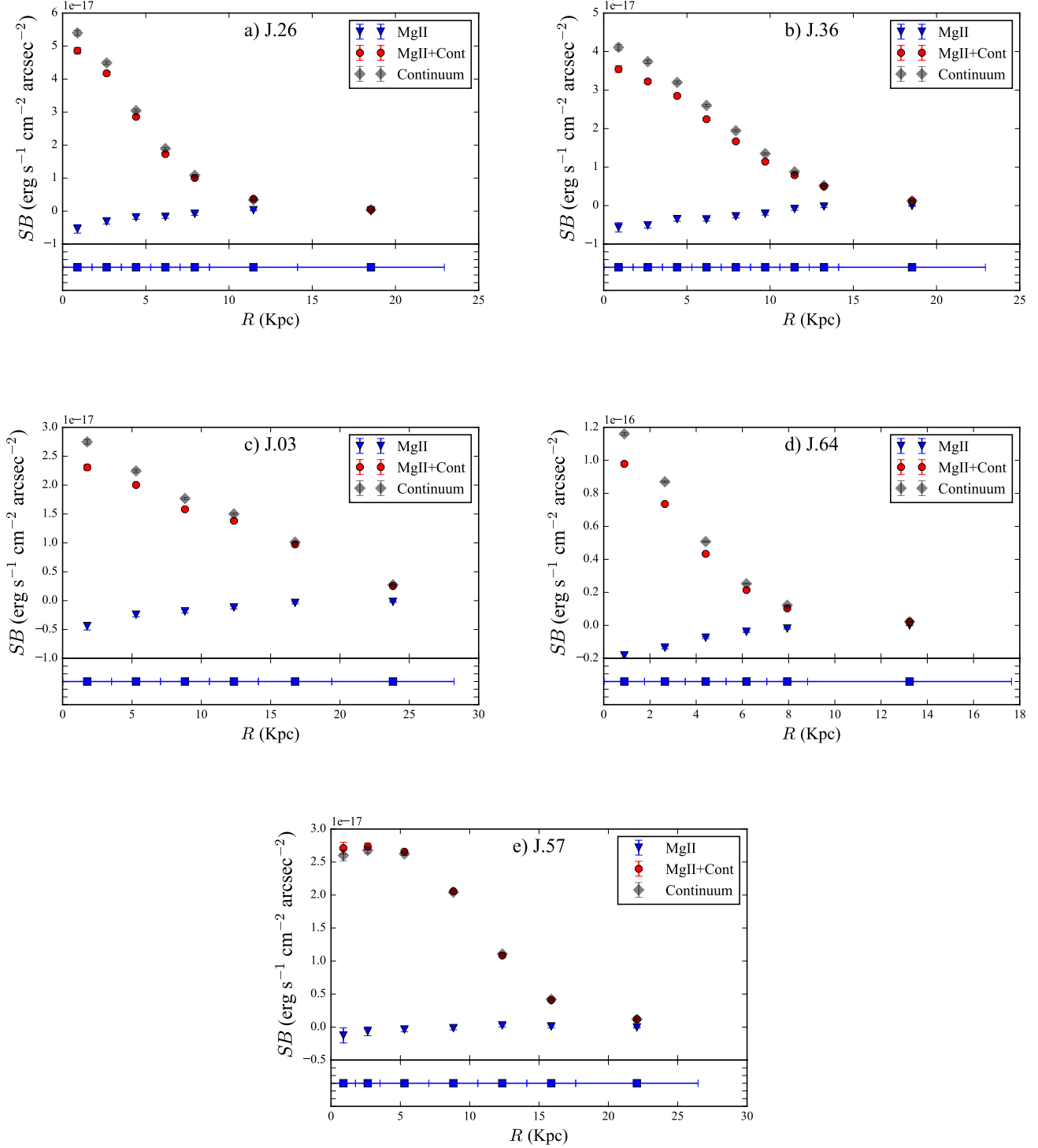


Figure 6. SB profiles for our sample galaxies. Top panels: Continuum SB profile (gray) measured for each galaxy. The red points show the Mg II + continuum SB measured for the galaxy in the pre-continuum-subtracted image. The blue points show the Mg II line SB measured in the continuum-subtracted line emission image. The profile exhibits SB decrements from Mg II absorption. Photometry was performed in circular annuli. Bottom panel: The vertical hashes show the inner and outer radii of each annulus in kpc. The distance from the center of the galaxy is marked with filled squares and is computed using the average value of the inner and outer radii of each annulus.

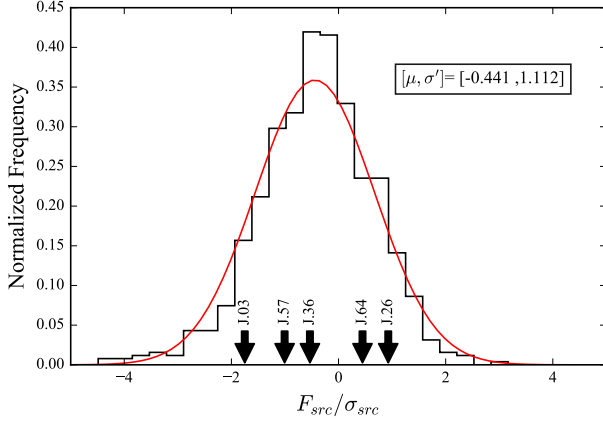


Figure 7. Normalized distribution of $F_{\text{src}}/\sigma_{\text{src}}$ values for random circular annuli placed on the continuum-subtracted line image. F_{src} is the total flux within an aperture and σ_{src} is the expected 1σ flux limit in the ideal case of perfect sky and continuum subtraction, i.e. $SB_1\sqrt{A_{\text{src}}}$. The black arrows point to the statistical significance of the flux inside the “extended annulus” of each galaxy.

Table 3. Significance of extracted flux and detection limits.

Object	$F_{\text{src}}(\text{Mg II})^a$	$5SB_{\text{limit}}^b$	Area ^c
J033225.26-274524.0	2.44(0.92)	6.51	21
J033232.36-274725.0	-1.40(-0.53)	6.51	21
J033230.03-274347.3	-5.23(-1.75)	5.74	27
J033229.64-274242.5	1.23(0.44)	6.22	26
J033230.57-274518.2	-2.53(-1.00)	6.81	18

^aMg II flux is in units of 10^{-18} ergs sec⁻¹ cm⁻². The value in parentheses is the statistical significance with respect to σ_{src} .

^bLimits are in units of 10^{-19} ergs sec⁻¹ cm⁻² arcsec⁻².

^cArea of the extended annulus in arcsec².

imaging, we simulate emission with varying intensities of SB_{limit} . For each galaxy, we assign our simulated emission a constant surface brightness corresponding to 1, 3, 5, 10 and 20 times the 1σ SB_{limit} inside the largest annulus used (i.e., the extended annulus). We assume Gaussian noise with 1σ equal to $1SB_{\text{limit}}$. Next, we subtract the continuum in the same manner as explained in Section 3.2.

To aid in identifying the presence and detectability of extended Mg II emission, we construct a χ_{smooth} , for each level of simulated emission, following the techniques in Hennawi & Prochaska (2013) and Arrigoni Battaia et al. (2015).

To construct this smoothed image, we first performed the following operation on a continuum-subtracted image:

$$I_{\text{smooth}} = \text{CONVOLVE}[\text{line-continuum}], \quad (3)$$

where the CONVOLVE operation indicates convolution of the Mg II images with a Gaussian kernel with FWHM=1.5 pixels. Next, we computed the sigma image, σ_{smooth} , by convolving the propagated error image:

$$\sigma_{\text{smooth}} = \sqrt{\text{CONVOLVE}^2[\sigma^2]}, \quad (4)$$

where the CONVOLVE² operation indicates convolution of the image with the square of the Gaussian kernel. The smoothed χ image is then the product of the data image divided by the sigma image.

$$\chi_{\text{smooth}} = \frac{I_{\text{smooth}}}{\sigma_{\text{smooth}}}. \quad (5)$$

Figure 8 shows the χ_{smooth} images for the 5 levels of simulated Mg II emission. We also include the χ_{smooth} image of each galaxy without any simulated emission (in the left-most column). The galaxies are outlined by a black isophotal contour corresponding to $1SB_1$ and the simulated emission is contained inside the extended annulus surrounding each contour. The χ_{smooth} images confirm that we should be able to detect extended Mg II emission down to a conservative level of $5SB_{\text{limit}}$.

4.3. Equivalent Widths

Here we derive an expression to calculate the equivalent width (EW_{MgII}) of any absorption or emission features observed in our narrow-band imaging. Starting from the expression for EW used in the context of spectroscopy,

$$EW_{\lambda} = \int \left(1 - \frac{f_{\lambda}}{f_{\text{cont}}}\right) d\lambda \quad (6)$$

we begin by dividing Eq 2 by the flux density of the continuum and the FWHM of the on-line filter,

$$\frac{F_{\lambda}}{f_{\text{cont}}\Delta\lambda_{\text{MgII}}} = \frac{F_{\text{MgII}}}{f_{\text{cont}}\Delta\lambda_{\text{MgII}}} - 1. \quad (7)$$

Next, we rearrange the above expression such that we produce the argument of the integrand in Eq. 6 on the right hand side,

$$-\frac{F_{\lambda}}{f_{\text{cont}}\Delta\lambda_{\text{MgII}}} = 1 - \frac{f_{\text{MgII}}}{f_{\text{cont}}}. \quad (8)$$

We then approximate the integration in Eq. 6 by multiplying the integrand above by the FWHM of the on-line filter $d\lambda = \Delta\lambda_{\text{MgII}}$,

$$-\frac{F_{\lambda}}{f_{\text{cont}}} = \left(1 - \frac{f_{\text{MgII}}}{f_{\text{cont}}}\right)\Delta\lambda_{\text{MgII}}; \quad (9)$$

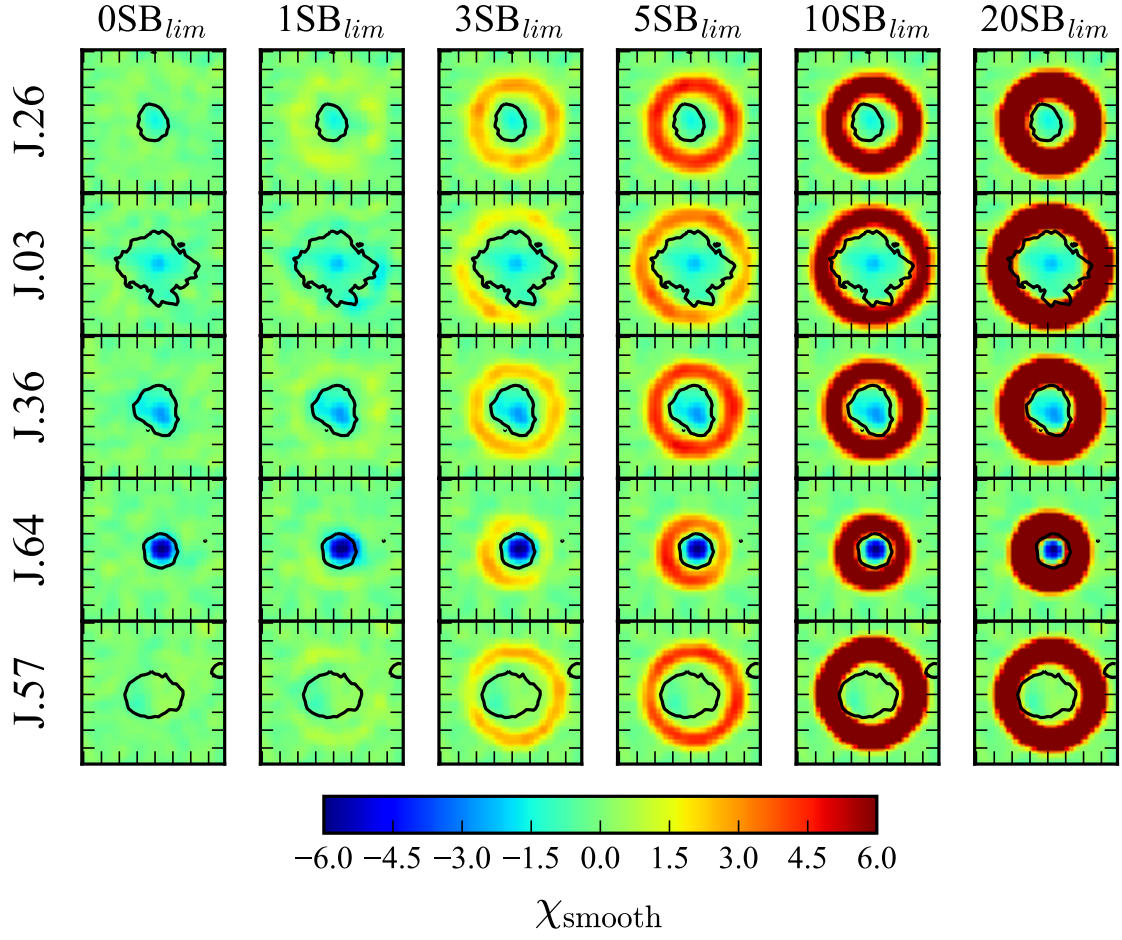


Figure 8. Continuum-subtracted χ_{smooth} images of the 5 galaxies in our sample. Every galaxy is placed in the same row in each column. The columns show simulated emission, with brightnesses of 0, 1, 3, 5, 10, and 20 times SB_{lim} . Each image has a size of $5'' \times 5''$ (corresponding to $35 \text{ kpc} \times 35 \text{ kpc}$ at $z \sim 0.70$). Each image shows the galaxy along with the same isophotal contour used in previous figures (in black).

such that

$$EW_{\text{MgII}} = -\frac{F_{\text{MgII}}}{f_{\text{cont}}}. \quad (10)$$

Using the above equation along with the continuum and continuum-subtracted images, we produce images of the observed-frame EW_{MgII} . The observed-frame EW_{MgII} images are displayed for each galaxy in Figure 9 and show only the EWs within the 1σ SB_1 contours of the corresponding Mg II images (prior to continuum subtraction).

To compare our map of $EW_{\text{Mg II}}$ to the values measured from the Keck/LRIS spectra, we place 0.9 arcsec-wide apertures over each galaxy. The width and position angle of the apertures are consistent with the orientation of the slits used to obtain the spectra. Next, we determine which pixels lie outside the 1σ SB_1 contours and set their values to zero. Outside this contour, the $EW_{\text{Mg II}}$ values become poorly constrained due to the lack of S/N in the continuum. We then select all pixels with a $S/N \geq 1.5$ within each slit aperture and create a histogram to show the distribution of their $EW_{\text{Mg II}}$ values. The histograms are shown in Figure 9. We also compute the mean equivalent width of these pixels and report their values in Table 4.

To assess the morphology of the Mg II absorption, we determine the projected distance of each pixel from the center of each galaxy in kiloparsecs. We plot the EW_{MgII} vs. this projected distance for each galaxy in the right panels of Figure 9. Although some of the plots suggest a slight upward trend in the values of EW_{MgII} with increasing radii, we cannot be confident in this trend because of the large scatter. To better visualize the data and test the significance of the trend, we bin the data radially in 3-5 kpc-wide bins. For example, in Figure 9(c), the absorption $EW_{\text{Mg II}}$ in J.03 extends out to ~ 25 kpc (shown in black in the right-most panel). The EW_{MgII} values are binned in 5 kpc increments. We calculate the mean and scatter of the $EW_{\text{Mg II}}$ in each bin and show these values in red in the right panels of Figure 9 and in 10.

5. RESULTS

5.1. Limits on Mg II Emission

For our sample of galaxies, we are sensitive to extended emission in annuli at projected distances of 18, 18, 24 and 14 kpc from the centers of J.26, J.36, J.03 and J.64, respectively. We do not detect any significant Mg II emission at these distances around any of our target galaxies. The χ_{smooth} images shown in Figure 8 confirm this. A comparison of the simulated emission with the χ_{smooth} version of the original continuum-subtracted image, shown in the first column, similarly suggests that

we do not detect any extended Mg II emission. We thus place 5σ upper limits on the SB of Mg II emission for each galaxy in the sample, summarized in Table 3. The most sensitive detection limit using the largest area is $SB(\text{Mg II}) < 5.74 \times 10^{-19} \text{ ergs sec}^{-1} \text{ cm}^{-2} \text{ arcsec}^{-2}$, computed for the galaxy J.03.

5.2. Spatially Resolved Maps of Mg II Absorption

In this section we discuss the details of the absorption detected in our SB profiles as well as compare our EW_{MgII} measurements to those measured in the supplemental Keck/LRIS spectra.

5.2.1. Effects of Mg II Absorption on Surface Brightness Profiles

Although we do not detect any extended Mg II emission, we do observe a decrement of flux, SB_{abs} , in the SB profiles of 4 out of 5 galaxies in our sample. As shown in Figure 6, absorption from Mg II ions is prevalent in the profiles at projected distances $\lesssim 5$ kpc, and decreases radially outward from the maximum absorption at the center of the galaxies. In Table 4 we report for the galaxies J.26, J.36 and J.03 a maximum decrement in the SB profile due to absorption ($SB_{\text{abs}} \approx -5 \times 10^{-18} \text{ erg s}^{-1} \text{ cm}^{-2} \text{ arcsec}^{-2}$). Additionally, we report for galaxy J.64 a SB_{abs} with a significantly more negative value of $(-18.2 \pm 0.1) \times 10^{-18} \text{ erg s}^{-1} \text{ cm}^{-2} \text{ arcsec}^{-2}$. Finally, for J.57, the value of $SB_{\text{abs}} = (-1.25 \pm 1.12) \times 10^{-18} \text{ erg s}^{-1} \text{ cm}^{-2} \text{ arcsec}^{-2}$, and is consistent with measuring zero absorption as expected given the redshift of this system. This measurement suggests that the quality of our continuum subtraction is satisfactory.

5.2.2. Morphology of MgII Absorption

Figure 9 shows the images, distributions and radial projections of Mg II EWs. We have zeroed out any values that lie outside the SB_1 contours for each galaxy. We also impose a signal-to-noise cut, only including $EW_{\text{Mg II}}$ values in the middle and right panels for pixels in which the continuum S/N is greater than 1.5. The mean $EW_{\text{Mg II}}$ is computed for all pixels inside each Keck/LRIS aperture, defined in Sec. 4.3, and the error is propagated in quadrature. The resulting values of the mean EW and the error of the measurements are summarized in Table 4. Comparing our narrowband EWs with those measured from the spectra, we find agreement to within 1.6-4.6 σ for galaxies J.26 and J.36, and more statistically significant differences for galaxies J.03 and J.64. We discuss possible causes for these differences below. We also note here that given the size of the median seeing disk for these observations ($\text{FWHM} \approx 0.8''$), the $EW_{\text{Mg II}}$ values measured in adjacent pixels (each of which subtends $0.25''$) are not independent, and hence

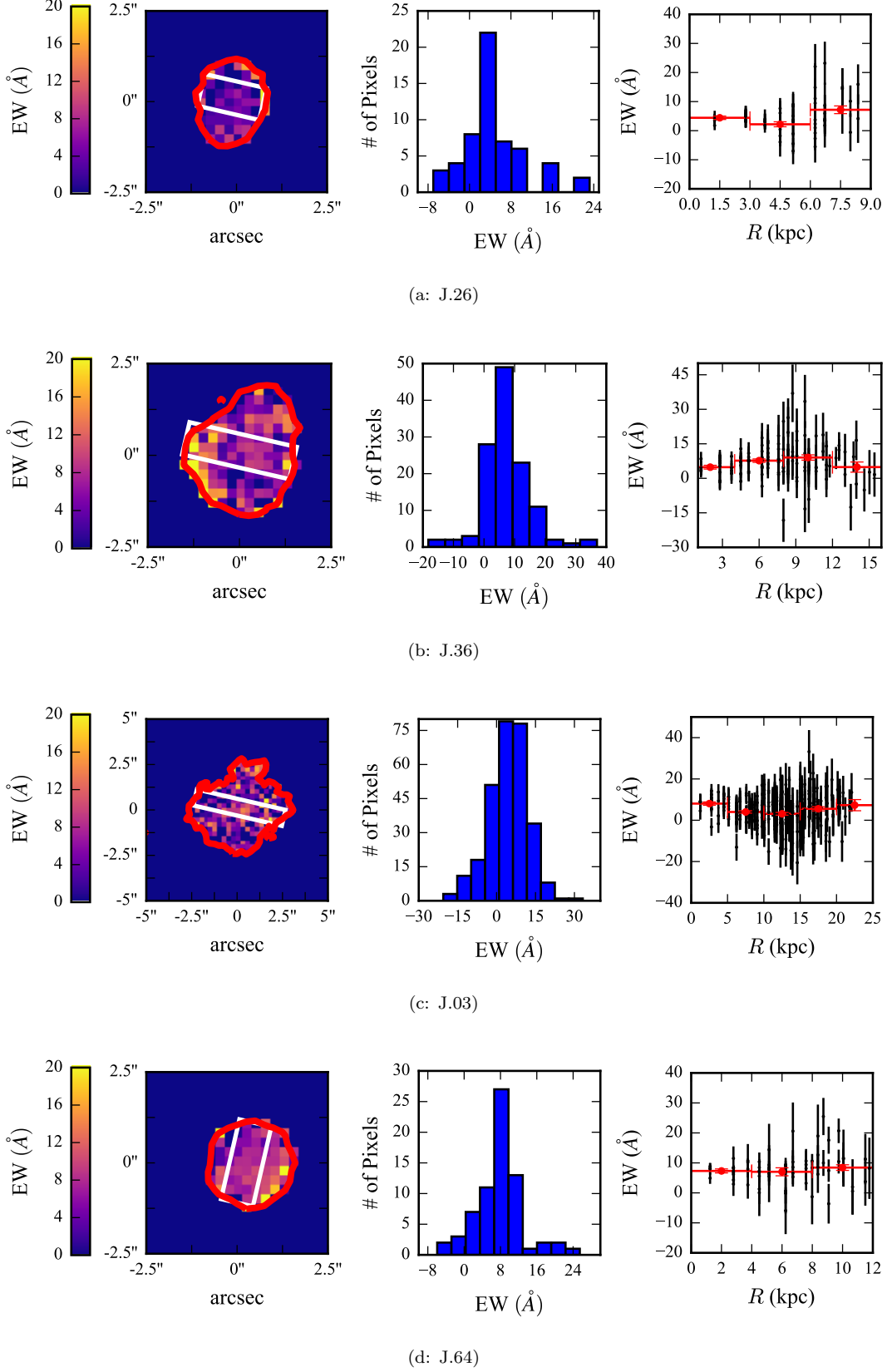


Figure 9. Left: Images of the equivalent widths $EW_{\text{Mg II}}$ inside the 1SB₁ contour for each galaxy (red). The white contour shows the placement and orientation of the 0.9''-wide slit used to measure the equivalent width of absorption in the Keck/LRIS spectrum of each galaxy. Middle: Distribution of $EW_{\text{Mg II}}$ values in pixels with continuum S/N > 1.5 inside the slit aperture. Right: The $EW_{\text{Mg II}}$ values of these high-S/N pixels vs. projected distance from the galaxy center are shown in black, and binned $EW_{\text{Mg II}}$ measurements are shown in red. The horizontal error bars represent the width of the radial bin used.

their errors are covariant. This covariance implies that the uncertainties in our mean $\text{EW}_{\text{Mg II}}$ values are underestimated, such that the discrepancies between these values and those measured in our LRIS spectra are likely less significant than the tension described above.

Figure 2(c) shows the Keck/LRIS spectrum of galaxy J.03. The continuum observed near the Mg II transition has low S/N compared to the spectra of the rest of the sample. Since the value of $\text{EW}_{\text{Mg II}}$ depends on the level of the continuum, it may well be that our choice of continuum level in calculating the $\text{EW}_{\text{Mg II}}$ from the spectrum is higher than the continuum level implied by our narrow-band image.

Figure 2(d) shows the Keck/LRIS spectrum of galaxy J.64. This object is the brightest galaxy in the sample, and also exhibits the highest-velocity wind. This shifts the Mg II absorption profile toward the blue end of the HeII+47 transmission curve, which could cause the signal in this filter to be dominated by the continuum level and the absorption signal to be underestimated.

As demonstrated in our radially-binned EW profiles, a majority of the galaxies exhibit large scatter in the binned $\text{EW}_{\text{Mg II}}$ at large radii. To better understand the significance of these trends, we compile the mean $\text{EW}_{\text{Mg II}}$ values for all the galaxies and show their profiles in Figure 10. To account for the varying sizes of the galaxies, we normalize the radii of the bins by the approximate radius of the SB_1 contour for each galaxy. Upon inspection of this figure, we see that the galaxies exhibit no statistically significant trend in the mean absorption $\text{EW}_{\text{Mg II}}$ as a function of radius inside our 1SB_1 isophotal contour, which suggests that the covering fraction is approximately constant across the surface.

6. DISCUSSION

6.1. Previous Detections of Extended Mg II Emission

Previous constraints on the brightness of scattered Mg II emission were reported by Rubin et al. (2011). In this work the authors studied emission from the starburst galaxy TKRS 4389 at $z = 0.69$ with a SFR of $49.8 M_{\odot} \text{ yr}^{-1}$. This emission was detected in a 2-dimensional Keck/LRIS spectrum, with flux from the emission reaching (8.0 ± 0.4) and $(4.4 \pm 0.4) \times 10^{-18} \text{ ergs sec}^{-1} \text{ cm}^{-2}$ at λ_{2796} and (4.0 ± 0.3) and $(2.5 \pm 0.4) \times 10^{-18} \text{ ergs sec}^{-1} \text{ cm}^{-2}$ at λ_{2803} in two independent locations spatially offset from the galaxy continuum. The flux from both emission lines can be converted into two surface brightness values by taking the average of the flux measured at each location and each transition, and dividing by a 1 arcsec^2 aperture.

Figure 11 shows each galaxy's 5σ SB detection limit and the SB calculated for the galaxy TKRS 4389 vs.

Table 4. Properties of Mg II Absorption

Object	SB_{abs}^a	$R_{\perp}^{\text{SB}_1 b}$ (kpc)	LRIS $\text{EW}_{\text{Mg II}}^{\text{obs} c}$ (Å)	NB $\text{EW}_{\text{Mg II}}^{\text{obs} d}$ (Å)
J.26	-5.4 ± 1.2	8	7.5 ± 0.4	3.5 ± 0.8
J.36	-5.6 ± 0.1	15	5.8 ± 0.5	7.7 ± 1.0
J.03	-4.4 ± 0.6	21	12.7 ± 1.7	5.4 ± 0.7
J.64	-18.2 ± 0.1	10	13.2 ± 0.3	7.6 ± 0.7
J.57	-1.3 ± 1.2	11	6.10 ± 0.4	-0.7 ± 0.6

^a Maximum SB decrement in units of $10^{-18} \text{ erg sec}^{-1} \text{ cm}^{-2} \text{ arcsec}^{-2}$.

^b Radius of SB_1 contour.

^c Measured from Keck/LRIS spectra in the observed frame. Includes both lines in the Mg II doublet.

^d Measured from narrowband images, and reported in the observed frame.

SFR (left panel) and vs. $\log M_*/M_{\odot}$ (middle panel). These figures suggest that we should be able to detect scattered Mg II emission with strengths similar to that detected in TKRS 4389 in our narrowband imaging. Taken at face value, the left panel of Figure 11 could be consistent with a positive correlation between Mg II SB and SFR. Future observations are needed to verify this trend, and the possibility that objects with yet higher SFRs ($\gtrsim 50 M_{\odot} \text{ yr}^{-1}$) exhibit brighter Mg II emission. The middle panel of Figure 11 suggests that extended Mg II emission may be brighter in lower mass galaxies. Both Erb et al. (2012) and Feltre et al. (2018) observed a similar trend in their examination of the total Mg II emission strength vs. galaxy M_* . Finally, the right panel of Figure 11 shows that the galaxy with detected Mg II also has the highest specific SFR. If it is ultimately confirmed that low- M_* galaxies with the highest SFRs, or highest specific SFRs, exhibit the brightest emission, this could point to a physical link between the escape velocity of galaxies and the spatial extent of wind material.

6.2. Geometry of Scattering Material

In the context of the idealized models of cool gas outflows discussed in Prochaska et al. (2011), radiative transfer calculations predict that strong Mg II emission will always accompany the blueshifted Mg II absorption that is ubiquitously observed to trace galactic-scale winds (Weiner et al. 2009; Martin et al. 2012; Rubin et al. 2014). For isotropic and dust-free scenarios, photons are conserved, as any absorbed continuum photon is eventually re-emitted. Therefore, the total equivalent

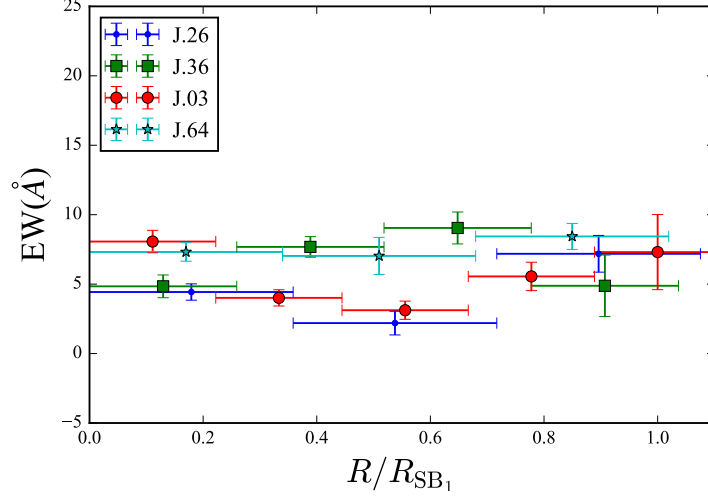


Figure 10. Radial profile of the mean EW of Mg II absorption for four of our sample galaxies. Profiles for J.26, J.36, J.03, and J.64 are shown with blue points, green squares, red circles, and cyan stars, respectively. The mean EW values are the same as those shown in the right column of Figure 9. We have normalized the corresponding radii by the approximate size of the SB₁ contour of each galaxy.

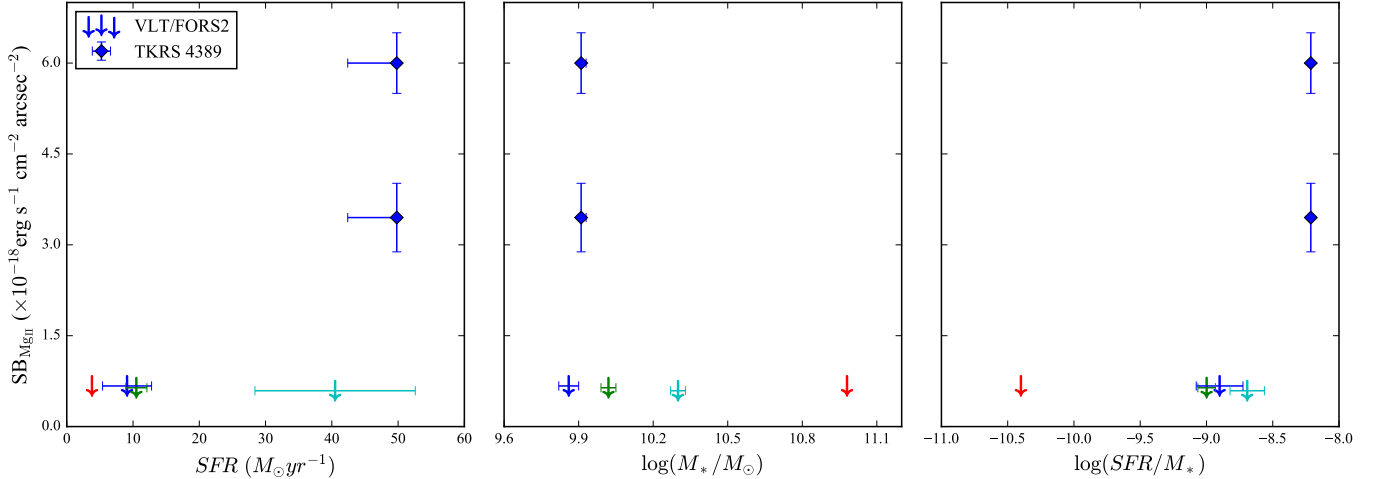


Figure 11. Comparison of our detection limits to the measured SB of extended Mg II emission around the starburst galaxy TKRS 4389. These surface brightness constraints are plotted vs. SFR (left), stellar mass (middle), and specific SFR (right). Our imaging is sufficiently sensitive to detect extended emission at similar strengths to the extended emission measured for TKRS 4389 with $SFR \sim 50 M_{\odot} \text{ yr}^{-1}$. The symbol colors indicate the same galaxies as in Figure 10

width of both the absorption and emission features is equal to zero in such models. Assuming that our galaxies host an isotropic and dust-free wind, we wish to determine how much emission is predicted to be generated by this wind, and how the SB of this emission compares to our detection limits.

To calculate the predicted emission flux we first determine the flux absorbed by Mg II ions. Using our Keck/LRIS spectra, we find the average value of the continuum near the Mg II doublet and multiply this value by the observed EW of the doublet. Then to estimate

the SB, we distribute this flux uniformly inside multiple annuli of varying sizes. These annuli all have an inner radius equal to the galaxy's isophotal radius and successively larger outer radii. Additionally, since our SB limits are dependent on the size of the aperture used, we calculate the SB detection limits of our images inside each of the aforementioned annuli. Figure 12 shows how the predicted SB of emission varies with the spatial extent of the annulus (red octagons), as well as how the SB compares with our detection limits (thin black curve). Excepting galaxy J.03, the predicted SB of this

emission lies above our detection limits. Under the assumption that the wind in these galaxies does in fact extend beyond the SB_1 isophotal contour (at $R_{\perp}^{\text{SB}_1} = 8\text{--}21$ kpc), the absence of the predicted emission, calculated from an isotropic wind model, in our narrowband imaging suggests that these galaxies do not host isotropic, dust-free winds.

6.2.1. Anisotropic, Dust-Free Winds

There are many phenomena that may reduce the SB of the scattered Mg II emission so that it is consistent with our observations. One factor that can affect the observed emission strength is the morphology of the wind. Anisotropic winds were shown in Prochaska et al. (2011) to exhibit reduced emission strengths compared to isotropic winds. Direct evidence for anisotropic winds, and specifically for a bipolar morphology, has been observed in emission from cold and shock-heated gas around local starburst galaxies (e.g., Walter et al. 2002; Westmoquette et al. 2008; Strickland & Heckman 2009). Around distant galaxies, enhanced Mg II absorption along a galaxy’s minor axis (Bordoloi et al. 2011; Kacprzak et al. 2012; Bouché et al. 2012) observed toward background QSO sightlines is likewise suggestive of bipolar outflows. Furthermore, the analysis of Rubin et al. (2014) demonstrating a strong dependence of the incidence of winds observed “down the barrel” on galaxy orientation was interpreted as additional, strong evidence for such a morphology.

We now assume that the brightness of emission in our galaxies is reduced by the effect of anisotropy. For the anisotropic winds modeled in Prochaska et al. (2011), the emission is reduced by the factor $\Omega/4\pi$, where Ω is the angular extent of the wind. As Prochaska et al. (2011) noted, given that the outflow must cover most of the continuum in order to be detected in typical down-the-barrel spectroscopy, the value of Ω has an approximate lower limit of $\Omega > 2\pi$. We show the predicted SB profiles for wind emission from our galaxies assuming $\Omega = 2\pi$ with gray diamonds in Figure 12.

After reducing the SB of the expected Mg II emission by the corresponding factor of 2, we predict profiles that fall below our SB detection limits for galaxies J.26 and J.36. However, the SB profile of J.64 remains above our detection limits, suggesting additional phenomena are needed to reduce the strength of scattered emission. As discussed in Section 5, this object is the brightest in our sample and exhibits the strongest Mg II absorption, which suggests the presence of a strong ISM component. Prochaska et al. (2011) noted that Mg II photons can be more effectively trapped in such objects with large amounts of dusty interstellar material.

6.2.2. Anisotropic, Dusty Winds

Dust in the wind is another factor that can reduce the observed emission strength and affect the shape of the Mg II line profile. In the Prochaska et al. (2011) models that include dust in the wind material, the dominant effect is that the most redshifted emission is suppressed. The line flux is reduced by a factor of $(1 + \tau_{\text{dust}})^{-1}$, where τ_{dust} is the integrated opacity of dust.

The MAGPHYS SED modeling of the sample galaxies performed by Rubin et al. (2014) provides an estimate of the dust opacity in the ISM of each system (shown in Table 1). We make the simplifying assumption that the wind has the same dust opacity as the ISM, and predict the SBs for an anisotropic wind with this level of dust opacity using the SB reduction factor given above. These values are shown with blue triangles in Figure 12. For the galaxies J.26, J.36 and J.03, the introduction of dust reduces the predicted emission yet further below our detection limits. For galaxy J.64, in which anisotropy alone did not reduce the predicted emission below our detection limits, Figure 12 shows that a combination of dust and anisotropy is sufficient to reduce the predicted strength of scattered emission so that it is consistent with our observational constraints.

7. CONCLUSION

We have presented the results of a narrowband imaging search for Mg II emission around a sample of five star-forming galaxies at a redshift of $z \sim 0.70$ which are known to exhibit outflows traced in Mg II absorption. We did not detect any Mg II emission in this sample, and place upper limits on the surface brightness in the range $\text{SB}(\text{Mg II}) < (5.74 - 6.81) \times 10^{-19} \text{ ergs sec}^{-1} \text{ cm}^{-2} \text{ arcsec}^2$ at 5σ significance. These limits are determined within annuli with areas of $\sim 20 \text{ arcsec}^2$, and having mean radii ranging from 13 to 24 kpc relative to the centers of each target. Our imaging also spatially resolves the strength of the Mg II absorption observed against the galaxy continua, yielding novel constraints on the Mg II absorption morphology. This absorption fully covers the galaxies from their centers out to isophotal contours defined by the 1σ depth of a continuum + Mg II image (at $R_{\perp}^{\text{SB}_1} = 8 - 21$ kpc), suggesting that the absorbing gas is optically thick and completely covers the stellar disks out to this distance. Additionally, radial profiles of the mean EW_{MgII} measured for our sample galaxies suggest that the EWs are approximately constant across the galaxies’ stellar surfaces.

We compared our surface brightness detection limits with the predictions of the radiative transfer models of Prochaska et al. (2011). If the winds in these galaxies do extend beyond the stellar disk, $\lesssim 20$ kpc, then

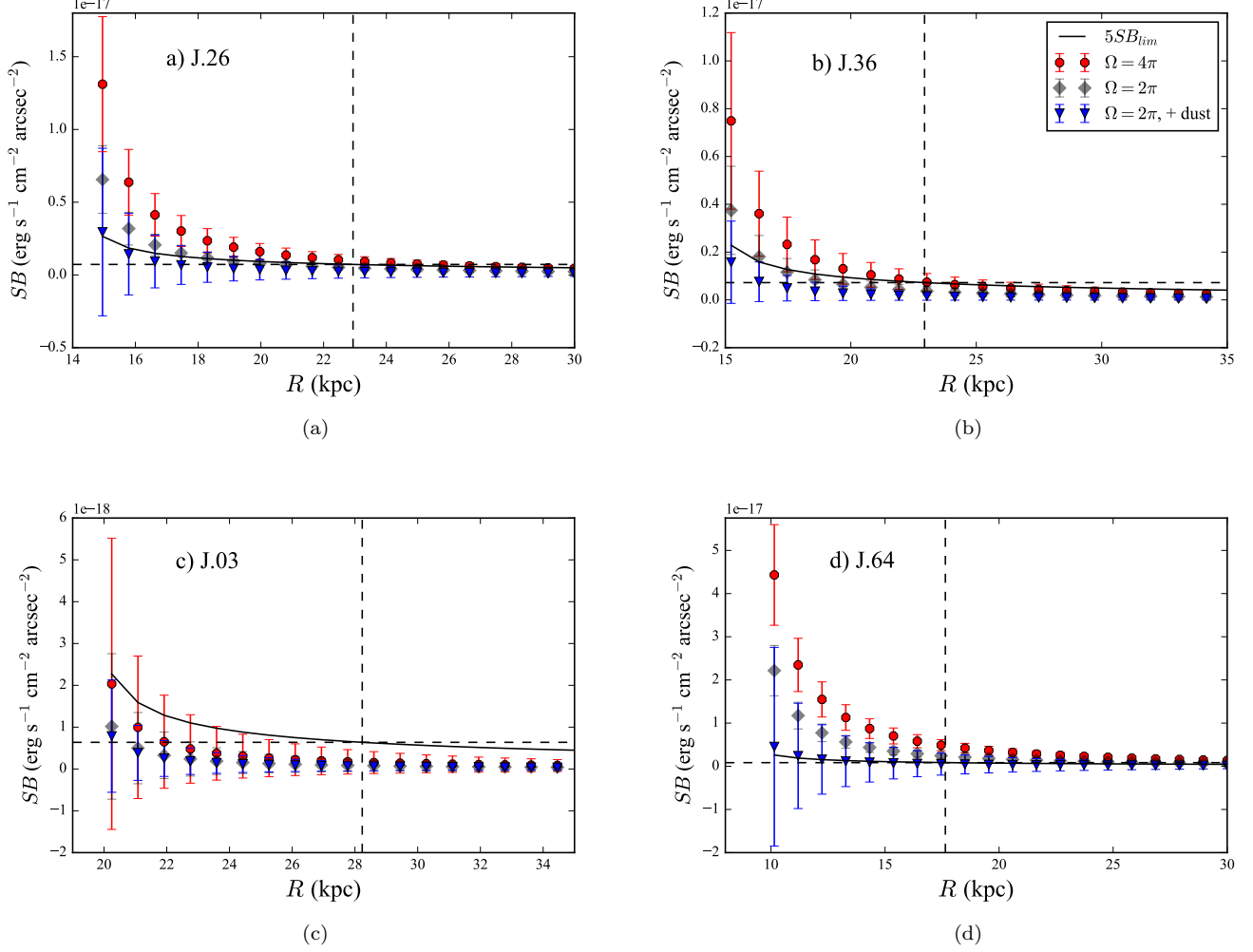


Figure 12. Predicted SB of Mg II emission for isotropic, anisotropic, and both anisotropic and dusty winds. The red octagons show the expected SB of emission that has been uniformly distributed inside an annulus (with inner radius equal to that of the galaxy's SB_1 contour and an outer radius equal to the x-axis value) for an isotropic wind. The gray diamond points show the SB of Mg II emission predicted for an anisotropic wind with angular extent $\Omega = 2\pi$. The blue triangles mark the predicted SB for a wind that is both anisotropic and affected by dust as described in the text. The solid line shows the value of our SB detection limits. The dashed vertical and horizontal lines represent the outer radius of the extended annulus used to measure the primary detection limits reported for each galaxy and the value of that limit. The legend in panel (b) holds for the remaining panels.

we are able to rule out that the winds in our sample are isotropic and dust free, as our images are sufficiently sensitive to detect the emission predicted by such models. Adopting the assumption of dusty and/or anisotropic winds reduces the strength of the predicted Mg II emission to lie below our detection limits. Although these limits suggest that the winds in our sample are not isotropic and dust-free, questions linger regarding the relative roles wind anisotropy, dust content, and extent play in reducing scattered emission. Thus, deeper imaging or spatially-resolved spectroscopy of Mg II will be needed to fully characterize the morphology of these winds.

R.R.V gratefully thanks Joe Burchett, Karin Sandstrom and Jessica Werk for enlightening discussions which improved this work. K.H.R.R. acknowledges support from the Alexander von Humboldt foundation in the context of the Humboldt Postdoctoral Fellowship. The Humboldt foundation is funded by the German Federal Ministry for Education and Research.

These findings are in part based on observations collected at the European Organisation for Astronomical Research in the Southern Hemisphere under ESO programs 090.A-0427(A).

REFERENCES

- Arrigoni Battaia, F., Yang, Y., Hennawi, J. F., et al. 2015, *ApJ*, 804, 26
- Bertin, E., Mellier, Y., Radovich, M., et al. 1996, *A&AS*, 117, 393
- Bohlin, R. C., Mészáros, S., Fleming, S. W., et al. 2017, *AJ*, 153, 234
- Bordoloi, R., Lilly, S. J., Knobel, C., et al. 2011, *ApJ*, 743, 10
- Bouché, N., Hohensee, W., Vargas, R., et al. 2012, *MNRAS*, 426, 801
- Chen, H.-W., Wild, V., Tinker, J. L., et al. 2010, *ApJL*, 724, L176
- Chevalier, R. A., & Clegg, A. W. 1985, *Nature*, 317, 44
- da Cunha, E., Charlot, S., Dunne, L., Smith, D., & Rowlands, K. 2012, in *IAU Symposium*, Vol. 284, *The Spectral Energy Distribution of Galaxies - SED 2011*, ed. R. J. Tuffs & C. C. Popescu, 292–296
- da Cunha, E., Charlot, S., & Elbaz, D. 2008, *MNRAS*, 388, 1595
- Davis, M., Guhathakurta, P., Konidaris, N. P., et al. 2007, *ApJL*, 660, L1
- Erb, D. K., Quider, A. M., Henry, A. L., & Martin, C. L. 2012, *ApJ*, 759, 26
- Feltre, A., Bacon, R., Tresse, L., et al. 2018, *ArXiv e-prints*, arXiv:1806.01864
- Giavalisco, M., Ferguson, H. C., Koekemoer, A. M., et al. 2004, *ApJL*, 600, L93
- Hennawi, J. F., & Prochaska, J. X. 2013, *ApJ*, 766, 58
- Jacoby, G. H., Quigley, R. J., & Africano, J. L. 1987, *PASP*, 99, 672
- Kacprzak, G. G., Churchill, C. W., & Nielsen, N. M. 2012, *ApJL*, 760, L7
- Kornei, K. A., Shapley, A. E., Martin, C. L., et al. 2013, *ApJ*, 774, 50
- Lang, D., Hogg, D. W., Mierle, K., Blanton, M., & Roweis, S. 2010, *AJ*, 139, 1782
- Larson, R. B. 1974, *MNRAS*, 169, 229
- Martin, C. L., Shapley, A. E., Coil, A. L., et al. 2012, *ApJ*, 760, 127
- Martin, C. L., Shapley, A. E., Coil, A. L., et al. 2013, *ApJ*, 770, 41
- Matsubayashi, K., Sugai, H., Hattori, T., et al. 2009, *ApJ*, 701, 1636
- Morton, D. C. 2003, *ApJS*, 149, 205
- Prochaska, J. X. 2016, *Linetools*, <https://github.com/linetools/linetools>
- Prochaska, J. X., Kasen, D., & Rubin, K. 2011, *ApJ*, 734, 24
- Rubin, K. H. R., Prochaska, J. X., Koo, D. C., et al. 2014, *ApJ*, 794, 156
- Rubin, K. H. R., Prochaska, J. X., Ménard, B., et al. 2011, *ApJ*, 728, 55
- Sarazin, M., & Roddier, F. 1990, *A&A*, 227, 294
- Springel, V., & Hernquist, L. 2003, *MNRAS*, 339, 289
- Strickland, D. K., & Heckman, T. M. 2009, *ApJ*, 697, 2030
- Sugahara, Y., Ouchi, M., Lin, L., et al. 2017, *ApJ*, 850, 51
- van Dokkum, P. G. 2001, *PASP*, 113, 1420
- Veilleux, S., Cecil, G., & Bland-Hawthorn, J. 2005, *ARA&A*, 43, 769
- Veilleux, S., Rupke, D. S. N., & Swaters, R. 2009, *ApJL*, 700, L149
- Walter, F., Weiss, A., & Scoville, N. 2002, *ApJL*, 580, L21
- Weiner, B. J., Coil, A. L., Prochaska, J. X., et al. 2009, *ApJ*, 692, 187
- Werk, J. K., Prochaska, J. X., Tumlinson, J., et al. 2014, *ApJ*, 792, 8
- Westmoquette, M. S., Smith, L. J., & Gallagher, J. S. 2008, *MNRAS*, 383, 864